

Antiferromagnetism and Kekulé valence bond order in the honeycomb optical Su-Schrieffer-Heeger-Hubbard model

Sohan Malkaruge Costa^{1,2}, Benjamin Cohen-Stead^{1,2} and Steven Johnston^{1,2}

¹*Department of Physics and Astronomy, The University of Tennessee, Knoxville, Tennessee 37996, USA*

²*Institute for Advanced Materials and Manufacturing, The University of Tennessee, Knoxville, Tennessee 37996, USA*

(Dated: November 27, 2025)

The precise role of electron-phonon (e -ph) coupling in graphene and related materials on a honeycomb lattice is not yet fully understood, despite extensive research on these systems. Here, we perform sign-problem-free determinant quantum Monte Carlo simulations of the optical Su-Schrieffer-Heeger (oSSH)-Hubbard model on the honeycomb lattice, focusing on the parameters relevant to graphene. Performing finite-size scaling analyzes, we obtain the model's ground state phase diagram, which includes the semi-metal (SM), Kekulé Valence Bond Solid (KVBS), and antiferromagnetic (AFM) phases, as well as indications of a small KVBS/AFM coexistence region. We find that a weak to moderate Hubbard repulsion, tuned toward the SM-AFM critical value in the pure honeycomb Hubbard model, enhances KVBS correlations and can even stabilize the KVBS phase. Estimating the effective parameters for graphene places it in the SM region of the phase diagram, but near the SM-KVBS phase boundary. Notably, we predict that increasing either the on-site Hubbard repulsion or the e -ph coupling strength drives graphene toward the KVBS phase rather than the AFM phase, highlighting a synergistic effect that can be exploited to further control the remarkable properties of graphene and related materials.

Introduction. The synthesis of single-layer graphene [1], and the subsequent discovery of superconductivity in magic-angle twisted bilayer graphene [2], has motivated extensive investigations of two-dimensional (2D) honeycomb systems [3–16]. These studies have focused on topics ranging from Dirac fermion physics [17], fractionalized quantum Hall effects [18], Moiré superlattices [2], topological phases [19], and the response to applied mechanical effects such as strain [20–23]. A variety of models have subsequently been proposed to describe the low-energy physics of graphene-based systems. For example, a series of studies has addressed the nature and location of a quantum critical point (QCP) in the honeycomb Hubbard model separating its semi-metal (SM) and antiferromagnetic (AFM) phases [4, 6, 15, 24]. There have also been studies investigating the emergence of charge-density-wave (CDW) order in the honeycomb Holstein model for electron-phonon (e -ph) interactions [7, 8] and its competition with AFM order when local Hubbard interactions are reintroduced [9].

An example of an experimentally observed emergent phenomena thought to involve both e -ph interactions and electronic correlations is the formation of Kekulé-O lattice distortions in strained graphene systems [16, 21, 23]. Several models incorporating electronic interactions give rise to a Kekulé Valence Bond Solid (KVBS) ground state consistent with the Kekulé-O order [25–27]. However, this phase is also accompanied by a corresponding lattice distortion [28], implying that the bond-stretching phonons may also play a role. This scenario is supported by angle-resolved photoemission experiments that have inferred strong e -ph coupling to graphene's bond-stretching optical phonons [28–31]. Given that Su-Schrieffer-Heeger (SSH)-like e -ph interactions have been linked to the emergence of Valence Bond Solid (VBS)

phases in various contexts [10, 32–40], including in the presence of competing electronic correlations [41], it is reasonable to expect they might also play an important role in the formation of Kekulé-O lattice distortions. Recent studies have shown just this, revealing that a KVBS phase emerges in honeycomb SSH models [13, 14]. However, these studies either neglected electronic correlations entirely [13] or only included the e -ph interaction at the mean-field level in the adiabatic limit [14].

Here we investigate the effects of both local Hubbard and optical Su-Schrieffer-Heeger (oSSH) interactions on a honeycomb lattice while treating both interactions on an equal footing. Specifically, we perform numerically-exact determinant quantum Monte Carlo (DQMC) simulations to study the competition between emergent KVBS and AFM correlations and map out the ground-state phase diagram as a function of the Hubbard and e -ph interaction strength at half-filling. Unlike previous studies, our DQMC calculations simulate fully quantum mechanical phonons, while also treating the electronic correlations exactly. We find that a Hubbard $U \lesssim 3.8t$ enhances KVBS correlations and lowers the critical e -ph coupling needed to stabilize this phase. We further find indications of a small KVBS-AFM coexistence region, which may reflect the presence of a weakly first-order phase transition between the two phases. By considering parameter values relevant for graphene, our results suggest that both e -ph and Hubbard-like interactions play a role in the emergence of Kekulé-O lattice distortions in strained graphene systems.

Model. The oSSH-Hubbard Hamiltonian on a honeycomb lattice can be conveniently partitioned as $\hat{H} =$

$\hat{H}_e + \hat{H}_{\text{ph.}} + \hat{H}_{e\text{-ph.}} + \hat{H}_{e\text{-e}}$. The first term

$$\hat{H}_e = -t \sum_{i,\nu,\sigma} \left[\hat{c}_{i+r_\nu,B,\sigma}^\dagger \hat{c}_{i,A,\sigma} + \text{h.c.} \right] - \mu \sum_{i,\gamma,\sigma} \hat{n}_{i,\gamma,\sigma} \quad (1)$$

is a noninteracting electron tight-binding Hamiltonian. Here $\hat{c}_{i,\gamma,\sigma}^\dagger$ ($\hat{c}_{i,\gamma,\sigma}$) creates (annihilates) a spin- σ electron on orbital $\gamma \in (A, B)$ of unit-cell i in the lattice, with $\hat{n}_{i,\gamma,\sigma} = \hat{c}_{i,\gamma,\sigma}^\dagger \hat{c}_{i,\gamma,\sigma}$ the corresponding number operator. The sum over r_ν ($\nu = 0, 1, 2$) runs over the three displacement vectors connecting an A orbital to its nearest-neighbors on sublattice B. The parameters t and μ are nearest-neighbor hopping amplitude and the chemical potential, respectively. Throughout this work, we consider a half-filled particle-hole symmetric system ($\mu = 0$), where the Fermi surface (FS) consists of a pair of Dirac points at $\mathbf{K}_\pm = \frac{2\pi}{a} \left(\frac{1}{3}, \pm \frac{1}{3\sqrt{3}} \right)$ and a is the lattice constant.

The second term in \hat{H} introduces the noninteracting lattice (phonon) degrees of freedom

$$\hat{H}_{\text{ph.}} = \sum_{i,\gamma} \left[\frac{\hat{P}_{i,\gamma}^2}{2M} + \frac{1}{2} M \Omega^2 \hat{R}_{i,\gamma}^2 \right]. \quad (2)$$

Here, we place two dispersionless optical phonon modes on each orbital to describe the in-plane motion of ions. Each phonon mode has frequency $\Omega = 0.1t$. The momentum and displacement operators for the pair of modes on each orbital are given by $\hat{\mathbf{P}}_{i,\gamma} = (\hat{P}_{i,\gamma,X}, \hat{P}_{i,\gamma,Y})$ and $\hat{\mathbf{R}}_{i,\gamma} = (\hat{X}_{i,\gamma}, \hat{Y}_{i,\gamma})$, respectively, with $\hat{P}_{i,\gamma} = |\hat{\mathbf{P}}_{i,\gamma}|$ and $\hat{R}_{i,\gamma} = |\hat{\mathbf{R}}_{i,\gamma}|$ and are defined such that the ion mass $M = 1$.

The third term in \hat{H} describes the e -ph coupling

$$\hat{H}_{e\text{-ph.}} = \alpha \sum_{i,\nu,\sigma} \Delta \hat{R}_{i,\nu} \left[\hat{c}_{i+r_\nu,B,\sigma}^\dagger \hat{c}_{i,A,\sigma} + \text{h.c.} \right], \quad (3)$$

where $\Delta \hat{R}_{i,\nu} = (\hat{\mathbf{R}}_{i+r_\nu,B} - \hat{\mathbf{R}}_{i,A}) \cdot \mathbf{r}_\nu / |\mathbf{r}_\nu|$ is the relative displacement of phonon modes on neighboring orbitals projected into the equilibrium bond direction. The e -ph interaction arises from an SSH-like coupling [42–44], where the lattice displacements linearly modulate the electron hopping energy, with the parameter α controlling the strength of the coupling. In the remainder of this paper we will report results in terms of a dimensionless e -ph coupling constant $\lambda = \alpha^2 / (M\Omega^2 t)$.

Finally, the last term is the local Hubbard repulsion

$$\hat{H}_{e\text{-e}} = U \sum_{i,\gamma} \left(\hat{n}_{i,\gamma,\uparrow} - \frac{1}{2} \right) \left(\hat{n}_{i,\gamma,\downarrow} - \frac{1}{2} \right), \quad (4)$$

where $U > 0$ controls the interaction strength.

Methods. We solve the model using DQMC simulations with hybrid Monte Carlo (HMC) updates to efficiently sample the phonon fields [45–48], as implemented in SmoQyDQMC.jl package [49, 50]. Because we are focusing on half-filling, the model has particle-hole symmetry

and the DQMC simulations are sign-problem-free [38]. Additional details of the DQMC simulations are provided in App. A

Based on previous work [9, 13–15], we expect the model to potentially host SM, AFM, and KVBS phases. The KVBS phase breaks a C_3 lattice-rotation symmetry while the AFM phase breaks $SU(2)$ spin-rotation symmetry. Their respective order parameters are given by

$$\hat{\Psi}_{\text{VBS}}(\mathbf{Q}) = \frac{1}{L^2} \sum_{j,\nu} e^{-i\mathbf{Q}\cdot\mathbf{j}} e^{-i2\pi\nu/3} \hat{B}_{j,\nu} \quad (5)$$

and

$$\hat{\Psi}_{\text{AFM}}(\mathbf{Q}) = \frac{1}{L^2} \sum_j e^{-i\mathbf{Q}\cdot\mathbf{j}} (\hat{S}_{j,A}^z - \hat{S}_{j,B}^z), \quad (6)$$

where $\hat{B}_{j,\nu} = \sum_\sigma \left(\hat{c}_{j+r_\nu,B,\sigma}^\dagger \hat{c}_{j,A,\sigma} + \text{h.c.} \right)$ and $\hat{S}_{i,\gamma}^z = \frac{1}{2} (\hat{n}_{j,\gamma,\uparrow} - \hat{n}_{j,\gamma,\downarrow})$ are the local bond and spin- z operators, respectively, and L the linear extent of the cluster in the direction of each lattice vector. The corresponding structure factors are $S_\theta(\mathbf{Q}) = L^2 |\hat{\Psi}_\theta(\mathbf{Q})|$, where $\theta = \text{AFM or VBS}$ denotes the type of order. The ordering wave-vectors for KVBS and AFM order are $\mathbf{Q} = \mathbf{K}_+$ and $\mathbf{\Gamma}$, respectively.

For finite-size scaling, we also measure the corresponding correlation ratio $R_\theta = 1 - \frac{1}{6} \sum_{\delta\mathbf{q}} S_\theta(\mathbf{Q} + \delta\mathbf{q}) / S_\theta(\mathbf{Q})$ associated with each structure factor, where $\delta\mathbf{q}$ denotes the six nearest-neighbor momentum points to the ordering wave-vector. Then, assuming Lorentz invariance, we take $\beta = Lt$ to project onto the ground-state [3, 4, 6, 51]. The crossing points of the correlation ratio curves as a function of the coupling for sequentially adjacent lattice sizes then provide an estimate of the critical coupling and can be used to locate a QCP.

Results. Figure 1 shows the ground state phase diagram for the half-filled oSSH-Hubbard model for $\Omega = 0.1t$, and constitutes our main result. It hosts Dirac SM, KVBS and AFM phases. We also find evidence for a small region of KVBS-AFM coexistence, which may reflect a weakly first-order transition that is difficult to fully resolve in the simulations.¹ The KVBS phase appears for large λ values, consistent with previous quantum Monte Carlo (QMC) investigations of the oSSH [13] and oSSH-Hubbard model in which the e -ph interaction is treated at a mean-field level [14]. The AFM phase appears for $U \gtrsim 3.8t$. The critical coupling U_c defining the AFM phase boundary varies weakly with the e -ph coupling for small λ ; however, once U_c crosses the KVBS transition line it is rapidly pushed to larger values with increasing λ . Interestingly, the onset of the AFM phase is accompanied by a dip in KVBS transition line and the emergence of a

¹ A similar coexistence region was also inferred for the square lattice Hubbard-oSSH model at finite temperatures [38].

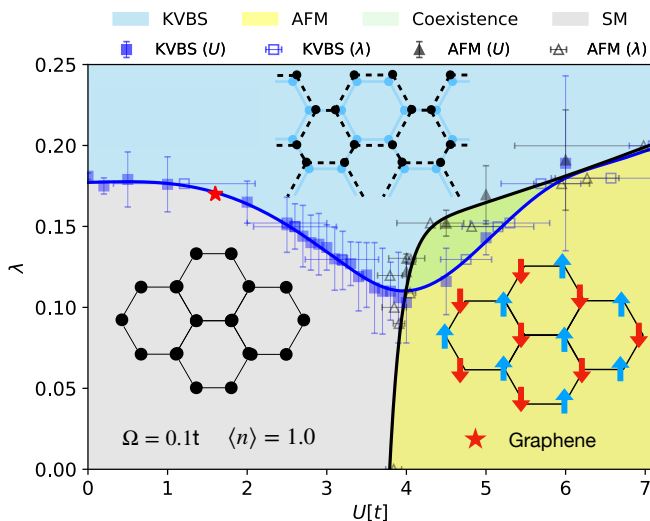


FIG. 1. Ground state $U - \lambda$ phase diagram for the Hubbard-oSSH model on a half-filled ($\langle n \rangle = 1$) honeycomb lattice, obtained for $\Omega = 0.1t$. Blue and black markers indicate a QCP for Kekulé valence bond solid (KVBS) and antiferromagnetic (AFM) phase transitions, respectively. Filled (empty) markers indicate the transition point found for fixed U (λ) to determine λ_c (U_c) for the relevant phase transition. Refer to Fig. 3 for examples of this analysis. The red star mark indicates the approximate location of graphene in the phase diagram. The blue and black lines are guides to the eye.

coexistence region for $U/t \in (3.8, 6.0)$ and $\lambda \in (0.11, 0.18)$. Notably, the minimal $\lambda_c \approx 0.11$ value occurs for a U value that roughly coincides with the QCP of the honeycomb Hubbard model ($U_c \approx 3.8t$ [4, 6, 15, 24]). We note that a similar dip in the KVBS λ_c phase boundary in proximity to the onset of the AFM phase was reported in Ref. [14] when treating the lattice at the mean-field level.

The red star in Fig 1 is the approximate location of unstrained graphene in the phase diagram if we assume the relevant phonon modes are the in-plane bond stretching A_1 and B_1 modes [13, 52, 53]; for more information refer to App. B. While graphene is placed in the SM region of the phase diagram, it is near the SM-KVBS phase boundary such that small perturbations that increase λ could easily stabilize the KVBS phase. This proximity was also observed in our previous work investigating the $U = 0$ limit of the oSSH-Hubbard model. Not only do our current results show that introducing a Hubbard interaction does not change this conclusion, but further suggest that increasing the effective U may also stabilize the KVBS phase. This result has important implications for engineering and manipulating graphene-based systems.

We now discuss the numerical results used to determine the phase diagram. Fig. 2 shows the structure factors $S_\theta(\mathbf{Q})$ as a function of U for fixed $\lambda = 0.13$ [panel (a)] and λ for fixed $U = 4.5t$ [panel (b)]. In both cases, we show results for $L = \beta t = 9$ and 12. For $\lambda = 0.13$ (Fig. 2a), the system passes through the SM, KVBS, coexistence, and AFM regions of the phase diagram as U increases.

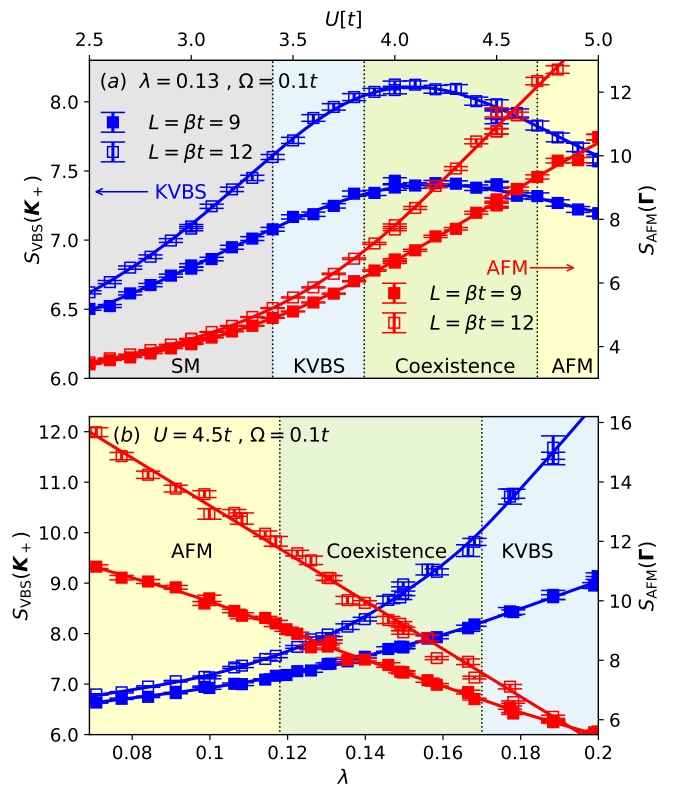


FIG. 2. The evolution of the KVBS $S_{VBS}(\mathbf{K}_+)$ and antiferromagnetic $S_{AFM}(\mathbf{\Gamma})$ structure factors for $\Omega = 0.1t$. Results are plotted as a function of (a) U for constant $\lambda = 0.13$ and (b) λ for constant $U = 4.5t$. The left [right] y -axis in both panels shows the $S_{VBS}(\mathbf{K}_+)$ [$S_{AFM}(\mathbf{\Gamma})$] values, as indicated by the arrows in the top panel. The colored regions indicate the four distinct regions in the phase diagram, including the coexistence region, consistent with Fig. 1. The blue and red lines are guides for the eye.

$S_{AFM}(\mathbf{\Gamma})$ increases monotonically with U along this cut through the phase diagram, while the $S_{VBS}(\mathbf{K}_+)$ structure factor exhibits non-monotonic behavior and peaks in the coexistence region. Additionally, the $S_{VBS}(\mathbf{K}_+)$ maximum shifts toward the boundary between the KVBS and coexistence region but remains within it with increasing lattice size L . This behavior suggests that the coexistence region may shrink in the thermodynamic limit, and could reflect the presence of a difficult to resolve weakly first-order phase transition. For larger U values, this coexistence region disappears entirely and the AFM and KVBS transition lines merge on the clusters accessed here, consistent with a direct transition between the two phases in the strong coupling regime.

Fig. 2b shows results for fixed $U = 4.5t$ as a function of λ , where system passes through the AFM, coexistence, and KVBS phases, respectively, while entirely avoiding the SM region of the phase diagram. Along this cut $S_{KVBS}(\mathbf{K}_+)$ monotonically increases and $S_{AFM}(\mathbf{\Gamma})$ monotonically decreases with λ , indicating that increases to λ effectively enhance KVBS correlations while suppressing AFM correlations. Additionally, both structure

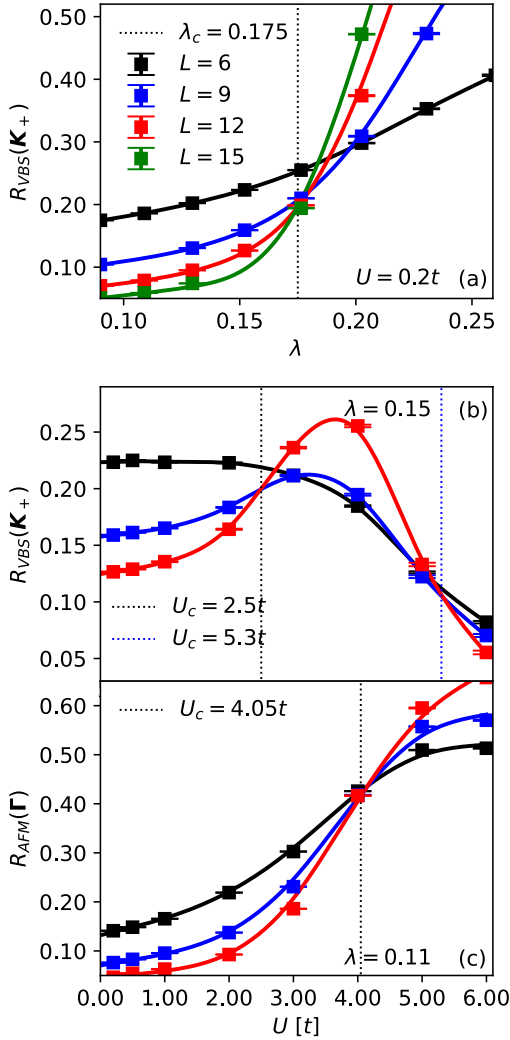


FIG. 3. A crossing analysis using the correlation ratios $R_{\text{VBS}}(\mathbf{K})$ and $R_{\text{AFM}}(\Gamma)$ to determine the QCP for the KVBS and AFM phases at $\Omega = 0.1t$. Here as we vary the lattice size, we set $\beta t = L$ to determine the location of the ground-state phase boundaries. (a) $R_{\text{VBS}}(\mathbf{K})$ vs. λ for fixed $U = 0.2t$. The QCP for the SM-KVBS phase transition is observed at $\lambda_c \approx 0.175$. (b) $R_{\text{VBS}}(\mathbf{K})$ vs U at $\lambda = 0.15$. Two crossing points are observed at $U_c \approx 2.5t$ and $5.3t$, indicating two QCPs for this value of the e -ph coupling strength. (c) $R_{\text{AFM}}(\Gamma)$ vs U for a constant $\lambda = 0.11$, with a QCP observed at $U \approx 4.05t$. Dashed lines in all panels indicate the estimated location of QCPs while the solid lines serve as guides to the eye.

factors show a pronounced dependence on system size, not only within their respective ordered regions of the phase diagram but also in the coexistence region, consistent with a long-range ordered state.

Figure 3 provides representative examples of both the AFM and KVBS correlation ratio crossings used to determine the phase boundaries in Fig. 1. In all cases, we consider $L = \beta t = 6, 9$, and 12 but include $L = \beta t = 15$ when needed. Fig 3a shows $R_{\text{VBS}}(\mathbf{K}_+)$ as a function of

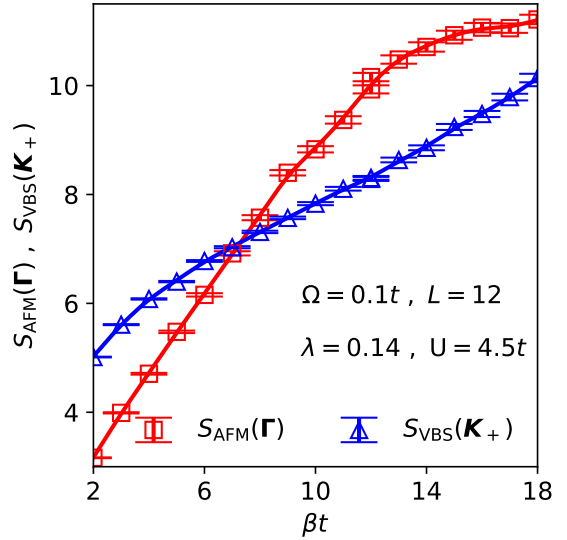


FIG. 4. AFM $S_{\text{AFM}}(\Gamma)$ (red \square) and KVBS $S_{\text{VBS}}(\mathbf{K}_+)$ (blue ∇) structure factors as a function of inverse temperature βt for an $L = 12$ lattice within the coexistence region of the phase diagram ($\Omega = 0.1t$, $U = 4.5t$, and $\lambda = 0.14$).

λ for $U = 0.2t$, in which we obtain the three crossing points λ_c^L for lattice size pairs $(L, L-3)$. The crossing points are well converged for λ_c^{15} ; therefore, we take $\lambda_c^{\text{KVBS}} \approx \lambda_c^{15} = 0.175$ as the critical coupling for the KVBS phase transition and estimate the corresponding uncertainty as $\Delta\lambda_c^{\text{KVBS}} = \pm|\lambda_c^{15} - \lambda_c^{12}| = \pm 0.005$. We use this approach to obtain all QCPs. Fig. 3b similarly shows the results for increasing U while keeping $\lambda = 0.15$ fixed. Here we observe two crossing points, the first one corresponding to the SM/KVBS transition and the second corresponding to the KVBS/AFM transition. Lastly, Fig. 3c shows the crossing point $U_c^{\text{AFM}}/t = 4.05 \pm 0.07$ for the QCP associated with an AFM transition at $\lambda = 0.15$.

Finally, Fig. 4 plots both the KVBS and AFM structure factors as a function of βt within the coexistence region of the phase diagram ($L = 12$, $\lambda = 0.14$ and $U = 4.5t$). We observe that both structure factors increase monotonically as the temperature is lowered, an indication of phase coexistence. Furthermore, $S_{\text{AFM}}(\Gamma)$ grows more quickly at high temperatures before gradually saturating at lower temperatures. Conversely, $S_{\text{VBS}}(\mathbf{K}_+)$ initially grows more slowly at high temperatures, and then more rapidly at lower temperature. There is an inflection point at approximately $\beta t \sim 10$, where the curves switches from concave down to concave up with decreasing temperature. Whether this coexistence would persist in the thermodynamic limit or is simply a signature of weakly first order transition is difficult to confidently discern on the finite sized lattices we are able to simulate.

Discussion. Prior DQMC work on the oSSH honeycomb model established the presence of a SM/KVBS transition at $\lambda_c \approx 0.18$ for quantum phonons and an en-

ergy $\Omega = 0.1t$ [13]. QMC studies have also identified a SM/AFM transition in the honeycomb Hubbard model at $U_c \approx 3.8t$ [4, 9, 51]. Our phase diagram in Fig. 1 is quantitatively consistent with these results, while also qualitatively resembling the phase diagram predicted in Ref. [14], which treated the phonons at the mean-field level. Interestingly, while U_c increases monotonically with λ , λ_c has a nonmonotonic dependence on U , with λ_c minimized for a Hubbard repulsions close to $U \approx 3.8t$. More specifically, introducing a small Hubbard interaction $U \lesssim 3.8$ effectively enhances the KVBS correlations. This is likely a result of the Hubbard interaction suppressing double occupancy and promoting short-range AFM correlations that favor local singlet formation consistent with the KVBS phase. We also observe indications of an AFM-KVBS coexistence region within a relatively small window $3.8t \leq U < 6t$. Whether this coexistence region persists in the thermodynamic limit, or is a result of finite size effects associated with a weakly first order transition, is difficult to discern at the lattice sizes we can access in our simulations.

First principles calculations place graphene in the SM region of the phase diagram but near SM-KVBS phase boundary. This location suggests that the system will be very sensitive to any external perturbations that increase either the effective on-site Hubbard repulsion or the strength of the e -ph interaction. Moreover, changes in these parameter are likely to drive graphene-based systems into the KVBS as opposed to AFM insulating phase. This result is consistent with experimental observations of strained graphene systems, where Kekulé-O lattice distortions are frequently observed [28]. Our results suggest that this phase could be manipulated either through strain engineering, modifying electronic screening channels, or pump-probe approaches to modifying U [54–56].

Acknowledgments — This work was supported by the National Science Foundation under Grant No. DMR-2401388.

Appendix A: Simulation parameters

We perform simulations on clusters ranging in size from $L = 6$ to 15. The number of orbitals for a given lattice

size is $N = 2L^2$. We typically performed an initial $\sim 5 \times 10^3$ HMC updates to thermalize the system, followed by an additional $\sim 1 \times 10^4$ updates, after each of which measurements were made. All simulations ran 8–12 parallel Markov chains to improve the measurement statistics. Throughout all the DQMC simulations, the imaginary-time discretization constant was set to $\Delta\tau = 0.05$. For the HMC updates, $N_t \sim 10$ time steps were performed, with the corresponding time-step size given by $\Delta t = \pi/(2\Omega N_t)$.

Throughout this work, we monitored the number of times that the SSH coupling results in an inversion of the sign of the hopping and ensured that it remained in the physical regime where the linear approximation is valid (i.e., below 1%) [13, 57].

Appendix B: Parameter Estimates for Graphene

The phonon modes in graphene that are thought to play an important role in the formation of KVBS correlations are the in-plane bond-stretching A_1 and B_1 optical modes, with energy $\Omega \approx 170\text{meV} = 0.065t$ [58–60]. In Ref. [13] we used *ab initio* calculations from Ref. [22] to estimate that microscopic e -ph coupling is $\alpha \approx 6.09 \text{ eV}/\text{\AA}$, with corresponding dimensionless e -ph coupling $\lambda \approx 0.17$. The phonon energy $\Omega = 0.1t$ used in this work is in the adiabatic regime relevant to graphene, and relatively close in value to the A_1 and B_1 energy. Additionally, in the adiabatic limit, the KVBS phase boundary is primarily controlled by λ , and is largely insensitive to the precise value of the phonon energy, provided that $\Omega/t \ll 1$ [13]. The effective Hubbard interaction $U \approx 1.6t$ for graphene is taken from Ref. [52], which used the Peierls-Feynman-Bogoliubov variational principle, in conjunction with comparisons to DQMC simulation results, to estimate a renormalized local Hubbard interaction that accounts for the effects of nonlocal Coloumb interactions.

-
- [1] K. S. Novoselov, A. K. Geim, S. V. Morozov, D. Jiang, Y. Zhang, S. V. Dubonos, I. V. Grigorieva, and A. A. Firsov, Electric field effect in atomically thin carbon films, *Science* **306**, 666 (2004).
 - [2] Y. Cao, V. Fatemi, S. Fang, K. Watanabe, T. Taniguchi, E. Kaxiras, and P. Jarillo-Herrero, Unconventional superconductivity in magic-angle graphene superlattices, *Nature* **556**, 43 (2018).
 - [3] I. F. Herbut, V. Juričić, and B. Roy, Theory of interacting electrons on the honeycomb lattice, *Phys. Rev. B* **79**, 085116 (2009).
 - [4] F. F. Assaad and I. F. Herbut, Pinning the order: The nature of quantum criticality in the Hubbard model on honeycomb lattice, *Phys. Rev. X* **3**, 031010 (2013).
 - [5] M. A. Sentef, M. Claassen, A. F. Kemper, B. Moritz, T. Oka, J. K. Freericks, and T. P. Devereaux, Theory of floquet band formation and local pseudospin textures in

- pump-probe photoemission of graphene, *Nature Communications* **6**, 7047 (2015).
- [6] F. Parisen Toldin, M. Hohenadler, F. F. Assaad, and I. F. Herbut, Fermionic quantum criticality in honeycomb and π -flux Hubbard models: Finite-size scaling of renormalization-group-invariant observables from quantum Monte Carlo, *Phys. Rev. B* **91**, 165108 (2015).
- [7] Y.-X. Zhang, W.-T. Chiu, N. C. Costa, G. G. Batrouni, and R. T. Scalettar, Charge order in the Holstein model on a honeycomb lattice, *Phys. Rev. Lett.* **122**, 077602 (2019).
- [8] C. Chen, X. Y. Xu, Z. Y. Meng, and M. Hohenadler, Charge-density-wave transitions of Dirac fermions coupled to phonons, *Phys. Rev. Lett.* **122**, 077601 (2019).
- [9] N. C. Costa, K. Seki, and S. Sorella, Magnetism and charge order in the honeycomb lattice, *Phys. Rev. Lett.* **126**, 107205 (2021).
- [10] M. Weber, Valence bond order in a honeycomb antiferromagnet coupled to quantum phonons, *Phys. Rev. B* **103**, L041105 (2021).
- [11] C.-X. Liu, Y. Chen, A. Yazdani, and B. A. Bernevig, Electron- k -phonon interaction in twisted bilayer graphene, *Phys. Rev. B* **110**, 045133 (2024).
- [12] C. D. Dashwood, A. Geondzhian, J. G. Vale, A. C. Pakpour-Tabrizi, C. A. Howard, Q. Faure, L. S. I. Veiga, D. Meyers, S. G. Chiuzbăian, A. Nicolaou, N. Jaouen, R. B. Jackman, A. Nag, M. García-Fernández, K.-J. Zhou, A. C. Walters, K. Gilmore, D. F. McMorrow, and M. P. M. Dean, Probing electron-phonon interactions away from the Fermi level with resonant inelastic x-ray scattering, *Phys. Rev. X* **11**, 041052 (2021).
- [13] S. Malkaruge Costa, B. Cohen-Stead, and S. Johnston, Kekulé valence bond order in the honeycomb lattice optical Su-Schrieffer-Heeger model and its relevance to graphene, *Phys. Rev. B* **110**, 115130 (2024).
- [14] Y. Otsuka and S. Yunoki, Kekulé valence bond order in the Hubbard model on the honeycomb lattice with possible lattice distortions for graphene, *Phys. Rev. B* **109**, 115131 (2024).
- [15] W. Kennedy, S. a. d. A. Sousa-Júnior, N. C. Costa, and R. R. dos Santos, Extended Hubbard model on a honeycomb lattice, *Phys. Rev. B* **111**, 155118 (2025).
- [16] E. Andrade, R. Carrillo-Bastos, and G. G. Naumis, Topical review: electronic and optical properties of Kekulé and other short wavelength spatial modulated textures of graphene, *Journal of Physics: Condensed Matter* **37**, 193003 (2025).
- [17] K. S. Novoselov, A. K. Geim, S. V. Morozov, D. Jiang, M. I. Katsnelson, I. V. Grigorieva, S. V. Dubonos, and A. A. Firsov, Two-dimensional gas of massless Dirac fermions in graphene, *Nature* **438**, 197 (2005).
- [18] K. I. Bolotin, F. Ghahari, M. D. Shulman, H. L. Stormer, and P. Kim, Observation of the fractional quantum Hall effect in graphene, *Nature* **462**, 196 (2009).
- [19] Y. Ren, Z. Qiao, and Q. Niu, Topological phases in two-dimensional materials: a review, *Reports on Progress in Physics* **79**, 066501 (2016).
- [20] G. G. Naumis, S. A. Herrera, S. P. Poudel, H. Nakamura, and S. Barraza-Lopez, Mechanical, electronic, optical, piezoelectric and ferroic properties of strained graphene and other strained monolayers and multilayers: an update, *Rep. Prog. Phys* **87**, 016502 (2023).
- [21] S. Sorella, K. Seki, O. O. Brovko, T. Shirakawa, S. Miyakoshi, S. Yunoki, and E. Tosatti, Correlation-driven dimerization and topological gap opening in isotropically strained graphene, *Phys. Rev. Lett.* **121**, 066402 (2018).
- [22] R. Ribeiro, V. M. Pereira, N. Peres, P. Briddon, and A. C. Neto, Strained graphene: tight-binding and density functional calculations, *New Journal of Physics* **11**, 115002 (2009).
- [23] D. Eom and J.-Y. Koo, Direct measurement of strain-driven Kekulé distortion in graphene and its electronic properties, *Nanoscale* **12**, 19604 (2020).
- [24] S. Sorella, Y. Otsuka, and S. Yunoki, Absence of a spin liquid phase in the Hubbard model on the honeycomb lattice, *Scientific reports* **2**, 992 (2012).
- [25] Z.-X. Li, Y.-F. Jiang, S.-K. Jian, and H. Yao, Fermion-induced quantum critical points, *Nature communications* **8**, 314 (2017).
- [26] X. Y. Xu, K. T. Law, and P. A. Lee, Kekulé valence bond order in an extended Hubbard model on the honeycomb lattice with possible applications to twisted bilayer graphene, *Phys. Rev. B* **98**, 121406 (2018).
- [27] Z.-X. Li, S. G. Louie, and D.-H. Lee, Emergent superconductivity and non-Fermi liquid transport in a doped valence bond solid insulator, *Phys. Rev. B* **107**, L041103 (2023).
- [28] H. Zhang, C. Bao, M. Schüler, S. Zhou, Q. Li, L. Luo, W. Yao, Z. Wang, T. P. Devereaux, and S. Zhou, Self-energy dynamics and the mode-specific phonon threshold effect in Kekulé-ordered graphene, *National Science Review* **9**, nwab175 (2021).
- [29] C. S. Leem, C. Kim, S. R. Park, M.-K. Kim, H. J. Choi, C. Kim, B. J. Kim, S. Johnston, T. Devereaux, T. Ohta, A. Bostwick, and E. Rotenberg, High-resolution angle-resolved photoemission studies of quasiparticle dynamics in graphite, *Phys. Rev. B* **79**, 125438 (2009).
- [30] F. Mazzola, J. W. Wells, R. Yakimova, S. Ulstrup, J. A. Miwa, R. Balog, M. Bianchi, M. Leandersson, J. Adell, P. Hofmann, and T. Balasubramanian, Kinks in the σ band of graphene induced by electron-phonon coupling, *Phys. Rev. Lett.* **111**, 216806 (2013).
- [31] M. X. Na, A. K. Mills, F. Boschini, M. Michiardi, B. Nosarzewski, R. P. Day, E. Razzoli, A. Sheyerman, M. Schneider, G. Levy, S. Zhdanovich, T. P. Devereaux, A. F. Kemper, D. J. Jones, and A. Damascelli, Direct determination of mode-projected electron-phonon coupling in the time domain, *Science* **366**, 1231 (2019).
- [32] S. Mazumdar, R. Clay, and H. Li, From valence bond solid to unconventional superconductivity in the organic charge-transfer solids, *Synthetic Metals* **159**, 2419 (2009), International Conference on Science and Technology of Synthetic Metals, Porto de Galinhas Pernambuco, Brazil, July 6-11, 2008.
- [33] H. Li, R. T. Clay, and S. Mazumdar, The paired-electron crystal in the two-dimensional frustrated quarter-filled band, *Journal of Physics: Condensed Matter* **22**, 272201 (2010).
- [34] X. Cai, Z.-X. Li, and H. Yao, Antiferromagnetism induced by bond Su-Schrieffer-Heeger electron-phonon coupling: A quantum Monte Carlo study, *Phys. Rev. Lett.* **127**, 247203 (2021).
- [35] A. Götz, S. Beyl, M. Hohenadler, and F. F. Assaad, Valence-bond solid to antiferromagnet transition in the two-dimensional Su-Schrieffer-Heeger model by Langevin dynamics, *Phys. Rev. B* **105**, 085151 (2022).

- [36] S. Malkaruge Costa, B. Cohen-Stead, A. T. Ly, J. Neuhaus, and S. Johnston, Comparative determinant quantum Monte Carlo study of the acoustic and optical variants of the Su-Schrieffer-Heeger model, *Phys. Rev. B* **108**, 165138 (2023).
- [37] A. Tanjaroon Ly, B. Cohen-Stead, S. Malkaruge Costa, and S. Johnston, Comparative study of the superconductivity in the Holstein and optical Su-Schrieffer-Heeger models, *Phys. Rev. B* **108**, 184501 (2023).
- [38] A. Tanjaroon Ly, B. Cohen-Stead, and S. Johnston, Antiferromagnetic and bond-order-wave phases in the half-filled two-dimensional optical Su-Schrieffer-Heeger-Hubbard model, *Phys. Rev. B* **111**, 245138 (2025).
- [39] M. Casebolt, C. Feng, R. T. Scalettar, S. Johnston, and G. G. Batrouni, Magnetic, charge, and bond order in the two-dimensional Su-Schrieffer-Heeger-Holstein model, *Phys. Rev. B* **110**, 045112 (2024).
- [40] J. L. Silva, G. Rein, S. d. A. Sousa-Júnior, F. F. Assaad, and N. C. Costa, The two-dimensional optical Su-Schrieffer-Heeger model: ground state and thermodynamic properties, [arXiv:2511.02707](https://arxiv.org/abs/2511.02707) (2025).
- [41] C. Feng, B. Xing, D. Poletti, R. Scalettar, and G. Batrouni, Phase diagram of the Su-Schrieffer-Heeger-Hubbard model on a square lattice, *Phys. Rev. B* **106**, L081114 (2022).
- [42] S. Barišić, J. Labbé, and J. Friedel, Tight binding and transition-metal superconductivity, *Phys. Rev. Lett.* **25**, 919 (1970).
- [43] W.-P. Su, J. Schrieffer, and A. Heeger, Soliton excitations in polyacetylene, *Physical Review B* **22**, 2099 (1980).
- [44] M. Capone, W. Stephan, and M. Grilli, Small-polaron formation and optical absorption in Su-Schrieffer-Heeger and Holstein models, *Phys. Rev. B* **56**, 4484 (1997).
- [45] S. Beyl, F. Goth, and F. F. Assaad, Revisiting the hybrid quantum Monte Carlo method for Hubbard and electron-phonon models, *Phys. Rev. B* **97**, 085144 (2018).
- [46] B. Cohen-Stead, O. Bradley, C. Miles, G. Batrouni, R. Scalettar, and K. Barros, Fast and scalable quantum Monte Carlo simulations of electron-phonon models, *Phys. Rev. E* **105**, 065302 (2022).
- [47] J. Ostmeyer, T. Nematiram, A. Troisi, and P. Buividovich, First-principles quantum Monte Carlo study of charge-carrier mobility in organic molecular semiconductors, *Phys. Rev. Appl.* **22**, L031004 (2024).
- [48] Minimal autocorrelation in hybrid Monte Carlo simulations using exact Fourier acceleration, *Computer Physics Communications* **313**, 109624 (2025).
- [49] B. Cohen-Stead, S. Malkaruge Costa, J. Neuhaus, A. Tanjaroon Ly, Y. Zhang, R. Scalettar, K. Barros, and S. Johnston, SmoQyDQMC.jl: A flexible implementation of determinant quantum Monte Carlo for Hubbard and electron-phonon interactions, *SciPost Phys. Codebases* , **29** (2024).
- [50] B. Cohen-Stead, S. Malkaruge Costa, J. Neuhaus, A. Tanjaroon Ly, Y. Zhang, R. Scalettar, K. Barros, and S. Johnston, Codebase release r0.3 for SmoQyDQMC.jl, *SciPost Phys. Codebases* , **29** (2024).
- [51] Y. Otsuka, S. Yunoki, and S. Sorella, Universal quantum criticality in the metal-insulator transition of two-dimensional interacting Dirac electrons, *Phys. Rev. X* **6**, 011029 (2016).
- [52] M. Schüler, M. Rösner, T. O. Wehling, A. I. Lichtenstein, and M. I. Katsnelson, Optimal hubbard models for materials with nonlocal coulomb interactions: Graphene, silicene, and benzene, *Phys. Rev. Lett.* **111**, 036601 (2013).
- [53] M. I. Katsnelson, *The Physics of Graphene*, 2nd ed. (Cambridge University Press, 2020).
- [54] N. Tancogne-Dejean, M. A. Sentef, and A. Rubio, Ultrafast modification of Hubbard U in a strongly correlated material: Ab initio high-harmonic generation in NiO, *Phys. Rev. Lett.* **121**, 097402 (2018).
- [55] D. R. Baykusheva, H. Jang, A. A. Husain, S. Lee, S. F. R. TenHuisen, P. Zhou, S. Park, H. Kim, J.-K. Kim, H.-D. Kim, M. Kim, S.-Y. Park, P. Abbamonte, B. J. Kim, G. D. Gu, Y. Wang, and M. Mitran, Ultrafast renormalization of the on-site Coulomb repulsion in a cuprate superconductor, *Phys. Rev. X* **12**, 011013 (2022).
- [56] O. Grånäs, I. Vaskivskiy, X. Wang, P. Thunström, S. Ghimire, R. Knut, J. Söderström, L. Kjellsson, D. Turenne, R. Y. Engel, M. Beye, J. Lu, D. J. Higley, A. H. Reid, W. Schlotter, G. Coslovich, M. Hoffmann, G. Kolesov, C. Schüßler-Langeheine, A. Styervoyedov, N. Tancogne-Dejean, M. A. Sentef, D. A. Reis, A. Rubio, S. S. P. Parkin, O. Karis, J.-E. Rubensson, O. Eriksson, and H. A. Dürr, Ultrafast modification of the electronic structure of a correlated insulator, *Phys. Rev. Res.* **4**, L032030 (2022).
- [57] D. Banerjee, J. Thomas, A. Nocera, and S. Johnston, Ground-state and spectral properties of the doped one-dimensional optical Hubbard-Su-Schrieffer-Heeger model, *Phys. Rev. B* **107**, 235113 (2023).
- [58] F. Wu, A. H. MacDonald, and I. Martin, Theory of phonon-mediated superconductivity in twisted bilayer graphene, *Phys. Rev. Lett.* **121**, 257001 (2018).
- [59] D. M. Basko, Effect of inelastic collisions on multiphonon raman scattering in graphene, *Phys. Rev. B* **76**, 081405 (2007).
- [60] D. M. Basko and I. L. Aleiner, Interplay of coulomb and electron-phonon interactions in graphene, *Phys. Rev. B* **77**, 041409 (2008).